

The Disk-Corona Model and Mass Estimates of the Ultraluminous X-ray Source Holmberg IX X-1

Ramandeep Gill,^{1,2,3*} Eda Sonbas,^{4,1} Kalvir S. Dhuga,¹ and Ersin Göğüş⁵

¹Department of Physics, The George Washington University, Washington, DC 20052, USA

²Department of Natural Sciences, The Open University of Israel, P.O. Box 808, Ra'anana 43537, Israel

³Astrophysics Research Center of the Open University (ARCO), The Open University of Israel, P.O. Box 808, Ra'anana 43537, Israel

⁴Adiyaman University, Department of Physics, 02040 Adiyaman, Turkey

⁵Faculty of Engineering and Natural Sciences, Sabancı University, Orhanlı - Tuzla, Istanbul 34956, Turkey

Received xxx; accepted xxx

ABSTRACT

The origin of the variable X-ray emission in the (0.3 – 30) keV energy range of ultraluminous X-ray sources (ULXs) remains unclear, making it difficult to constrain the mass of the central compact object. Many ULXs show X-ray luminosities, $L_X > 10^{39}$ erg s⁻¹, that exceed the Eddington limit (L_{Edd}) of stellar-mass black holes (BHs) commonly found in Galactic BH binaries. Sub-critical accretion ($L < L_{\text{Edd}}$) on to an intermediate-mass BH is one attractive scenario with the alternative being super-critical accretion on to a stellar-mass BH. Broadband X-ray emission in the former scenario can be explained using the canonical disk plus Comptonizing corona model, whereas in the latter scenario radiation pressure driven massive winds lead to complex spectra that are inclination angle dependent. Here we fit the broadband (optical/UV to X-ray) spectrum of the persistently bright ULX Holmberg IX X-1 with the disk-corona plus irradiated outer disk model in an effort to constrain the BH mass. We use a one-zone time-dependent numerical code to exactly solve for the steady-state properties of the optically thick coronal photon-electron-positron plasma. Our modelling suggests that Holmberg IX X-1 hosts a stellar mass BH, with mass $4 \lesssim (\dot{M}_{\text{BH}} \equiv \alpha M_{\text{BH}}/M_{\odot}) \lesssim 10$ where $1/6 \leq \alpha < 1$ for a spinning (Kerr) BH, undergoing super-critical accretion ($L_{\text{Bol}}/L_{\text{Edd}} \sim 20\alpha$). In our model, the X-ray spectrum below 10 keV is explained with an absorbed multi-colour disk spectrum having inner disk temperature $k_B T_{\text{in}} \sim (2.2 - 2.9)$ keV. An additional cooler thermal spectral component, as found in many works and not included in our modeling, is required. The hard excess above 10 keV, as seen by *NuSTAR*, arises in a photon-rich optically-thick Comptonizing spherical corona with optical depth $\tau_T \sim 3.5$ and particle temperature $k_B T_e \sim 14$ keV.

Key words: accretion – black hole physics – radiation mechanisms: non-thermal – radiative transfer – X-rays: binaries

1 INTRODUCTION

Ultraluminous X-ray sources (ULXs) are non-nuclear point sources found in nearby galaxies with X-ray luminosities, $L_X > L_{\text{Edd}} \approx 1.3 \times 10^{39} (M_{\text{BH}}/10M_{\odot})$ erg s⁻¹, in excess of the Eddington luminosity of a $10M_{\odot}$ stellar-mass black hole (BH) that is routinely observed in Galactic BH binaries (GBHB; see, e.g., reviews by Feng & Soria 2011; Kaaret et al. 2017). Owing to their flux variability on timescales of hours to years, the majority of ULXs are thought to be powered by accretion on to a compact object. At least six of them that showed X-ray pulsations were identified with having a neutron star (NS) accretor (Bachetti et al. 2014; Fürst et al. 2016; Israel et al. 2017a,b; Carpano et al. 2018; Sathyaprakash et al. 2019; Rodríguez Castillo et al. 2020). For the large number of remaining sources that do not show any pulsations, the mass of the compact object is a matter of intense debate. Two plausible scenarios have been offered to explain their super-Eddington luminosities: (i) Many of the more luminous sources with $L_X > 10^{40}$ erg s⁻¹ must be powered by sub-critical accretion on to an intermediate-mass black hole (IMBH)

with $M_{\text{BH}} \sim (10^2 - 10^4)M_{\odot}$ (e.g., Colbert & Mushotzky 1999; Makishima et al. 2000; Miller & Colbert 2004; Miller et al. 2004; Farrell et al. 2009), which can accommodate super-Eddington luminosities, and (ii) lower luminosity, but still super-Eddington, sources can be explained with super-critical accretion (e.g. Begelman 2002; Poutanen et al. 2007; Dotan & Shaviv 2011) on to a stellar-mass BH with $M_{\text{BH}} \sim (10 - 10^2)M_{\odot}$, in which a strong outflow can further boost the isotropic-equivalent luminosity by relativistic beaming (Ohsuga & Mineshige 2011). However, optical observations of extended highly ionized nebulae surrounding extremely luminous sources, e.g. Holmberg IX X-1, have placed strong constraints on relativistic beaming and instead favour isotropic emission (Moon et al. 2011).

The highly luminous ULXs typically display two spectral components in the (0.3–10) keV energy range (e.g., Miller et al. 2003; Vierdayanti et al. 2010; Miller et al. 2013), comprising of a softer quasi-thermal excess below 2 keV and a harder power-law component above that energy, where the latter also shows spectral curvature in the $\sim (3 - 10)$ keV energy range (e.g., Feng & Kaaret 2005; Stobbart et al. 2006; Gladstone et al. 2009; Walton et al. 2011). Apart from the spectral curvature, these are analogous to the two-component spec-

* E-mail: rsgill.rg@gmail.com

tra of GBHBs. In these sources, the softer component is modeled as multi-color disk (MCD) blackbody emission originating in the inner accretion disk, with characteristic temperature $k_B T_{\text{in}} \sim 1$ keV, where k_B is the Boltzmann constant, and the harder power-law is thought to arise in an optically thin (Thomson optical depth $\tau_T \lesssim 1$) Comptonizing corona (see [Remillard & McClintock 2006](#), for a review). When the same model is applied to ULXs it yields low disk temperatures with $k_B T_{\text{in}} \sim (0.1 - 0.3)$ keV (e.g., [Miller et al. 2003](#); [Cropper et al. 2004](#)) and an optically thick ($\tau_T > 6$) corona with electron temperature $k_B T_e \sim (1 - 2)$ keV. In a [Shakura & Sunyaev \(1973\)](#) accretion disk, the canonical model used to describe GBHBs, the inner disk temperature scaling $T_{\text{in}} \propto M_{\text{BH}}^{-1/4}$ implies that ULXs are indeed powered by IMBHs. One of the main hurdles for this interpretation is that it requires an unreasonably high mass being held in stellar clusters to explain the production efficiency of ULXs ([King 2004](#)).

The spectral curvature revealed by *XMM-Newton* in the $\sim (3 - 10)$ keV energy range was confirmed, as well as extended to energies above 10 keV, by *NuSTAR* observations that also revealed a spectral turnover (e.g. [Bachetti et al. 2013](#); [Walton et al. 2014](#)). These observations further revealed the necessity of an additional spectral component above 10 keV, often assumed to be a cutoff power law, when modelling the broadband spectra of several ULXs. Therefore, any continuum model that shows an exponential drop in flux density, namely a Wien spectral tail, at high energies has been found to be inconsistent with *NuSTAR* data of many ULXs (e.g. [Mukherjee et al. 2015](#); [Walton et al. 2015](#); [Luangtip et al. 2016](#); [Walton et al. 2017](#)). In addition, this extra spectral component has also been identified in ULXs with a bonafide NS accretor, thus providing tantalizing hints that other non-pulsating ULXs may also host NSs rather than BHs ([Pintore et al. 2017](#); [Koliopoulos et al. 2017](#); [Walton et al. 2018](#)).

To understand the origin of the broadband X-ray spectra of ULXs as well as characterize the spectral variability a variety of empirical models are used (e.g., [Stobbart et al. 2006](#)). The best fits to X-ray data below ~ 10 keV are provided by dual thermal models that feature some combination of pure blackbody and an MCD blackbody spectra ([Mitsuda et al. 1984](#)). Equally good or better fits are provided by physically motivated models featuring an accretion disk (e.g., DISKPN [Gierliński et al. 1999](#)) plus a Comptonizing corona spectrum obtained from self-consistent models, e.g. compTT ([Titarchuk 1994](#)) and EQPAIR ([Coppi 2000](#)). In many cases in which *NuSTAR* observations are used, the thermal models are supplemented by a cutoff power law model CUTOFFPL or a simple Comptonization model SIMPL ([Steiner et al. 2009](#)) to explain the hard excesses above 10 keV. All of these models constrain the properties of the accretion disk and the steady state corona, however, they do not provide any direct constraints on the mass of the compact object apart from the normalization of the disk component that does depend on M_{BH} .

In this work, we remedy this shortcoming by incorporating the mass of the accretor, assumed here to be a BH of mass M_{BH} , into the model parameters, yielding a more complex behavior, where it not only affects the overall normalization but also the spectral shape, thus making it more self-consistent. The underlying model builds on the successes of the two-component disk plus Comptonizing corona model, and just like EQPAIR, it allows for hybrid particle distributions, such as thermal plus non-thermal. However, being a time-dependent one-zone model it evolves the properties of the corona until it reaches a steady state and yields parameters like the Thomson optical depth (τ_T) and the particle temperature (T_e) rather than specifying it a priori for spectral fitting. In addition, the model allows to constrain the size of the corona, providing more insight into the geometry of the region that produces the harder spectral component.

Our model also includes the irradiated disk component, which is often missing in most works and has only been included in some (e.g. [Vinokurov et al. 2013](#)). Addition of this component allows for truly broadband fits that include optical/UV observations which yields further constraints on the accretion disk.

The rest of the paper is organized as follows. We present the formalism of the disk-corona model in §2 where we discuss the essential points and equations for the Comptonizing corona (§2.1), the disk component (§2.2), and the irradiated disk contribution (§2.3) to the total broadband spectrum. Our numerical treatment based on a one-zone time-dependent kinetic code is outlined in §3. Next, we present example model spectra, along with the corresponding coronal particle distribution, in §4 where we vary key model parameters to highlight their effect on the broadband spectrum. Constraining the mass of the central BH in the ULX Holmberg IX X-1 is the subject of §5 where we show that the X-ray observations favour a stellar-mass BH. We discuss the caveats and implications of our findings in §6 and conclude in §7.

2 THE DISK-CORONA MODEL

We consider an optically thick flat disk at a source distance D and inclination i that radiates a bolometric soft-photon flux $F_d = L_d \cos i / 2\pi D^2$. The disk luminosity is given by (e.g., [Makishima et al. 2000](#))

$$L_d = 4\pi(R_{\text{in}}/\xi)^2 \sigma_{\text{SB}}(T_{\text{in}}/\kappa)^4, \quad (1)$$

where T_{in} is the maximum disk color temperature, R_{in} is the innermost disk radius, and σ_{SB} is the Stefan-Boltzmann constant. The correction factor $\xi = 0.41$ corrects for the fact that the disk attains the color temperature T_{in} at a slightly larger radius than R_{in} (e.g., [Shimura & Takahara 1995](#)), and the factor $\kappa = T_{\text{in}}/T_{\text{eff}} \sim 1.7$ relates T_{in} to the effective temperature T_{eff} of the disk ([Kubota et al. 1998](#)). It is possible that these correction factors may change with the physical parameters of the system ([Merloni et al. 2000](#)). Here we identify R_{in} with the innermost stable circular orbit, such that $R_{\text{in}} = R_{\text{ISCO}} = 3\alpha R_s$ where $R_s = 2GM_{\text{BH}}/c^2$ is the Schwarzschild radius, M_{BH} is the mass of the BH, G is the gravitational constant, and c is the speed of light. The parameter $1/6 \leq \alpha \leq 1$ provides a generalization for spinning (Kerr) BHs with $\alpha = 1$ for non-spinning (Schwarzschild) BHs. It is convenient to express the disk luminosity using the mass of the BH, a more fundamental quantity, which gives

$$L_d = 7.3 \times 10^{34} \alpha^2 \left(\frac{\xi}{0.41}\right)^{-2} \left(\frac{\kappa}{1.7}\right)^{-4} \left(\frac{M_{\text{BH}}}{10M_{\odot}}\right)^2 \left(\frac{k_B T_{\text{in}}}{0.1 \text{ keV}}\right)^4 \text{ erg s}^{-1}. \quad (2)$$

The disk luminosity is intercepted by a spherical corona with size R_{cor} where it is Compton upscattered by a hybrid (thermal + non-thermal) electron-positron coronal plasma with Thomson optical depth τ_T . Here we make the generalization that the size of the corona is some fraction $\hat{R}_{\text{cor}} = R_{\text{cor}}/R_{\text{in}}$ of the inner disk radius. We express the disk luminosity using the compactness parameter, a non-dimensional quantity that combines the luminosity and radius of the emission region into one ([Guilbert et al. 1983](#)), such that

$$\begin{aligned} \ell_d &\equiv \frac{\sigma_T}{m_e c^3} \frac{(\Omega/4\pi)L_d}{R_{\text{cor}}} \\ &= \frac{0.2\alpha}{\hat{R}_{\text{cor}}} \left(\frac{\Omega}{4\pi}\right) \left(\frac{\xi}{0.41}\right)^{-2} \left(\frac{\kappa}{1.7}\right)^{-4} \left(\frac{M_{\text{BH}}}{10M_{\odot}}\right) \left(\frac{k_B T_{\text{in}}}{0.1 \text{ keV}}\right)^4, \end{aligned} \quad (3)$$

where the factor of $\Omega/4\pi$ is the fraction of disk luminosity intercepted by the corona assuming that the emission is isotropic. The corona subtends a solid angle $\Omega = 2\pi \left(1 - \sqrt{1 - \hat{R}_{\text{cor}}^2}\right)$, for $\hat{R}_{\text{cor}} \leq 1$, on to emitting material at a distance $R = R_{\text{in}}$ from its center, which is also the center of the accreting system. In the two limiting cases, $\Omega = 2\pi$ when $\hat{R}_{\text{cor}} = 1$ and $\Omega = \pi\hat{R}_{\text{cor}}^2$ when $\hat{R}_{\text{cor}} \ll 1$. Since most of the flux is emitted from $R \approx R_{\text{in}}$ as the disk temperature declines with increasing R (see §2.2), we further make the crude but simpler approximation that for $\hat{R}_{\text{cor}} > 1$, the solid angle is $\Omega = 4\pi$, so that the corona intercepts majority of the emitted disk luminosity. At large distances away from the corona, the solid angle is small and the corona intercepts only a very small fraction of emitted radiation. However, the contribution to the emitted flux also declines with R . A proper treatment of radiative transfer would require accounting for the radial and angular dependence of the disk emission, which cannot be done with a one-zone treatment, as adopted in this work. If $R_{\text{cor}} < R_{\text{in}}$, the spectrum should be dominated by emission arising from the disk, and therefore only show a sub-dominant Comptonized emission component. For the remaining discussion in this section and that in §3 and §4, we make the simplifying assumption that $R_{\text{cor}} > R_{\text{in}}$ and most of the disk emission is intercepted by the corona.

When the disk temperature is low, e.g. $k_B T_{\text{in}} = 0.1$ keV, the disk compactness of a stellar mass BH doesn't exceed unity with the implication that the corona remains optically thin to scattering. However, as the mass of the BH approaches that of IMBHs or if the disk becomes much hotter then $\ell_d \gg 1$. In this case, if a significant fraction of the radiation is emitted above the pair-creation threshold of $m_e c^2 = 511$ keV, where m_e is the electron rest mass, then pair-production by $\gamma\gamma \rightarrow e^+ + e^-$ becomes important and the reprocessing of the disk radiation by these pairs cannot be ignored. Another important consequence is the increase in optical depth of the pairs as ℓ_d becomes significantly larger than unity, which would make the corona optically thick if the compactness of the e^\pm -pairs (ℓ_e) is at least a modest fraction of the disk compactness.

2.1 The Comptonizing Corona

The corona is assumed to be loaded with e^\pm pairs that have a total compactness

$$\ell_e = \frac{\sigma_T}{m_e c^3} \frac{L_e}{R_{\text{cor}}}, \quad (4)$$

which is some fraction (ℓ_e/ℓ_d) of the disk photon compactness. The injected pairs can be non-thermal with power-law energy distribution having number density $n_e(\gamma_e) \propto \gamma_e^{-s}$ for $\gamma_m \leq \gamma_e \leq \gamma_M$, where $\gamma_e = (1 - \beta_e^2)^{-1/2}$ is the particle Lorentz factor bounded by γ_m and γ_M , the Lorentz factors of minimal and maximal energy particles, respectively. In some cases, when s is much larger than unity, e.g. for a very soft distribution, a delta-function is used instead. Magnetic fields are considered to be weak in the corona, and therefore, the pairs cool mainly by inverse-Compton scattering and synchrotron cooling is negligible.

Softer disk radiation with energy E_s is then inverse-Compton scattered by these e^\pm -pairs to higher energies $E_c = (4/3)\gamma_e^2 E_s$. The rate at which each electron is Compton cooled, thereby giving its energy to the scattered photon is $L_c = (4/3)\sigma_T c p_e^2 U_\gamma$, where $p_e \equiv \gamma_e \beta_e$ is the dimensionless momentum of the particle and U_γ is the radiation field energy density. Then the cooling rate for the entire distribution

of particles enclosed in a volume $(4\pi/3)R_{\text{cor}}^3$ is given by

$$L_c = \frac{4}{3}\sigma_T c U_\gamma \frac{4\pi}{3} R_{\text{cor}}^3 \int p_e^2 n_e(\gamma_e) d\gamma_e = \frac{16\pi}{9} R_{\text{cor}}^2 c U_\gamma \langle p_e^2 \rangle \tau_T \quad (5)$$

Here $\langle p_e^2 \rangle$ represents the average taken over the particle distribution and $\tau_T = n_{\text{tot}} \sigma_T R_{\text{cor}}$ is the Thomson optical depth of the corona with n_{tot} being the total number density of particles. The quantity that will become useful later is the ratio of the Comptonized luminosity of the corona to the luminosity of the softer disk radiation,

$$\frac{L_c}{L_d} = \frac{4\xi^2 \kappa^A \hat{R}_{\text{cor}}^2 c U_\gamma \langle p_e^2 \rangle \tau_T}{9\sigma_{\text{SB}} T_{\text{in}}^4}. \quad (6)$$

2.2 The Disk Spectrum

A soft excess below 2 keV appears in the spectra of many ULXs (e.g., Fabian & Ward 1993; Kaaret et al. 2003; Miller et al. 2003) that is typically fit by a cool MCD spectrum (Mitsuda et al. 1984) with inner disk temperature $k_B T_{\text{in}} \sim 0.1 - 0.3$ keV. A similar soft excess is also seen in GBHBs, but the corresponding inner disk temperature is much higher, $k_B T_{\text{in}} \sim 1$ keV.

The disk is assumed to be optically thick that radiates a multi-color blackbody spectrum for $R > R_{\text{in}}$ with a generalized radial temperature profile, where the local disk temperature scales with radial distance from the BH as a power law, such that $T(R) \propto R^{-p}$ (Minshige et al. 1994). For the canonical Shakura & Sunyaev (1973) disk $p = 3/4$. The disk spectrum for a power-law temperature profile can be obtained from (Mitsuda et al. 1984),

$$\dot{n}_\gamma(x) = \frac{dn_\gamma}{dx dt} = \left(\frac{dn_{\gamma,\text{inj}}}{dt}\right) x^2 \int_1^{\hat{R}_{\text{out}}} \frac{\hat{R}}{\exp[x/\theta(\hat{R})] - 1} d\hat{R}, \quad (7)$$

where $\dot{n}_\gamma(x)$ is the number density of photons per unit dimensionless energy per unit time. The photon energy E is expressed in dimensionless units, $x = E/m_e c^2$, and likewise, the dimensionless temperature of the disk blackbody radiation is

$$\theta(\hat{R}) = \frac{k_B T(\hat{R})}{m_e c^2} = \theta_{\text{in}} \hat{R}^{-p} \quad (8)$$

where θ_{in} is the temperature at the inner disk boundary at $\hat{R} = R/R_{\text{in}} = 1$. The total rate of photons is obtained by integrating the disk radiation up to the outer disk radius $\hat{R}_{\text{out}} = R_{\text{out}}/R_{\text{in}}$.

While the softer emission (below 2 keV) in the majority of ULXs is well described by an MCD spectrum, a subset of sources show a pure blackbody-like emission with temperature $k_B T \approx 0.05 - 0.2$ keV (e.g. Feng et al. 2016). In that case, the disk blackbody spectrum with temperature θ_{in} is given by

$$\dot{n}_\gamma(x) = \left(\frac{dn_{\gamma,\text{inj}}}{dt}\right) \frac{x^2}{\exp(x/\theta_{\text{in}}) - 1}, \quad (9)$$

where $dn_{\gamma,\text{inj}}/dt$ is again the rate per unit volume at which soft photons are entering the corona from the disk.

2.3 The Irradiated Disk

Besides viscous heating, accretion disks are also heated by intercepting the X-ray flux from the inner disk and the Comptonizing corona. Following Gierliński et al. (2009), we construct a simple model of disk irradiation, where a fraction f_{out} of the bolometric luminosity, $L_{\text{bol}} = L_d + L_c$, comprising of the inner disk and corona, is reprocessed by the outer disk. It is assumed here that the irradiating flux impinging at any given radius is given by

$$F_{\text{irr}} = \sigma T_{\text{irr}}^4(R) = \frac{L_{\text{bol}}}{4\pi R^2} = \frac{L_d}{4\pi R^2} f_{\text{out}} \left(1 + \frac{L_c}{L_d}\right), \quad (10)$$

where the disk luminosity is given by Eq. (2). Since the reprocessed radiation emitted by the outer disk is thermal, its temperature profile can now be expressed as

$$\theta_{\text{irr}}(\hat{R}) = \frac{[f_{\text{out}}(1 + L_c/L_d)]^{1/4}}{\kappa \xi^{1/2}} \theta_{\text{in}} \hat{R}^{-1/2}, \quad (11)$$

where the ratio L_c/L_d is given in Eq. (6) and is obtained self-consistently using the numerical treatment of the corona, as presented below.

3 NUMERICAL TREATMENT

We simulate the interactions between the photons and e^\pm -pairs using a one-zone kinetic code that solves the time-dependent coupled equations for isotropic and arbitrary distributions. The photons are initialized on a grid of dimensionless energy $x_{\text{min}} < x < x_{\text{max}}$ where the number density of photons per unit dimensionless energy at any time t is given by $n_\gamma(x, t) = \partial n_\gamma / \partial x$. Likewise, the e^\pm -pairs are initialized with a grid in dimensionless momentum with $p_{\text{min}} < p_e < p_{\text{max}}$ where their number density per unit dimensionless momentum is given by $n_\pm(p_e, t) = \partial n_\pm / \partial p_e$. Since the code has no spatial information, the simulated region, which represents the corona, is assumed to be spherical with radial extent R_{cor} . The code solves the following coupled equations,

$$\dot{n}_\gamma(x, t) = \dot{n}_{\gamma, \text{inj}}(x, t) + \dot{n}_{\gamma, \text{cs}}(x, t) + \dot{n}_{\gamma, \text{pp}}(x, t) + \dot{n}_{\gamma, \text{pa}}(x, t) + \dot{n}_{\gamma, \text{esc}}(x, t) \quad (12)$$

$$\dot{n}_\pm(p_e, t) = \dot{n}_{\pm, \text{inj}}(p_e, t) + \dot{n}_{\pm, \text{cs}}(p_e, t) + \dot{n}_{\pm, \text{pp}}(p_e, t) + \dot{n}_{\pm, \text{pa}}(p_e, t) + \dot{n}_{\pm, \text{coul}}(p_e, t), \quad (13)$$

where the different terms represent interaction rates per unit volume per unit dimensionless energy (momentum) for photons (particles) (see, e.g., Belmont et al. 2008; Belmont 2009; Vurm & Poutanen 2009; Gill & Thompson 2014, for the different rates and their numerical implementation). Both photons and particle equations include terms that represent the rates for injection (inj), Compton scattering (cs; $\gamma + e^\pm \rightarrow \gamma + e^\pm$), pair-production (pp; $\gamma + \gamma \rightarrow e^+ + e^-$), and pair-annihilation (pa; $e^+ + e^- \rightarrow 2\gamma$). Additional terms include an escape (esc) term for photons (particles don't escape the corona) and a Coulomb (coul; $e^+ + e^- \rightarrow e^+ + e^-$) interaction term for the particles.

The multi-color thermal emission emerging from the disk is intercepted by the corona where it is Comptonized by the e^\pm -pairs. The rate of injection of these thermal photons is set by the compactness, which in turn is set by the black hole mass M_{BH} and the fractional size of the corona \hat{R}_{cor} in Eq. (3), to give

$$\ell_d = \frac{4\pi\sigma_T}{3c} R_{\text{cor}}^2 \int \dot{n}_{\gamma, \text{inj}}(x) x dx, \quad (14)$$

where we have assumed a constant rate of injection. The above equation is then used to determine the normalization $dn_{\gamma, \text{inj}}/dt$ in Eq. (7 & 9) for a given θ_{in} , p , and \hat{R}_{out} .

The injection of e^\pm -pairs into the corona is determined in a similar manner, where the rate of injection (also assumed to be constant here) is controlled by the pair compactness,

$$\frac{\ell_e}{2} = \frac{4\pi\sigma_T}{3c} R_{\text{cor}}^2 \int \dot{n}_{\pm, \text{inj}}(p_e) \gamma_e dp_e. \quad (15)$$

Here the compactness also includes the rest mass of particles, and not just the kinetic energy, and the factor of (1/2) multiplying ℓ_e means that only half of the total compactness goes into each species (electron and positron) of particles. When considering a power-law energy distribution of pairs, such as $\dot{n}_\pm(p_e) = (p_e/\gamma_e) \dot{n}_\pm(\gamma_e) =$

$(p_e/\gamma_e)(dn_{\pm, \text{inj}}/dt)\gamma_e^{-s}$ for $\gamma_{\text{min}} \leq \gamma_e \ll \gamma_{\text{max}}$, the normalization $dn_{\pm, \text{inj}}/dt$ can be obtained from the above equation that yields

$$\frac{dn_{\pm, \text{inj}}}{dt} = \frac{3c}{8\pi\sigma_T} \frac{\ell_e}{R_{\text{cor}}^2} \left[\frac{s-2}{\gamma_{\text{min}}^{2-s} - \gamma_{\text{max}}^{2-s}} \right] (s > 2). \quad (16)$$

For a delta-function injection of pairs with distribution $\dot{n}_\pm(p_e) = (p_e/\gamma_e)(dn_\pm/dt)\delta(\gamma_e - \gamma_0)$, the rate of injection is given by

$$\frac{dn_{\pm, \text{inj}}}{dt} = \frac{3c}{8\pi\sigma_T} \frac{\ell_e}{R_{\text{cor}}^2 \gamma_0}, \quad (17)$$

where γ_0 is the energy per unit rest mass energy per particle of the injected pairs.

The Comptonized radiation continuously escapes the corona with rate

$$\dot{n}_{\gamma, \text{esc}}(x, t) = -\kappa(x, t) \frac{n_\gamma(x, t)}{t_{\text{dyn}}}, \quad (18)$$

where we use the standard ‘leaky-box’ approximation under which the radiation leaks out with an escape probability $\kappa(x, t)$ over the dynamical time $t_{\text{dyn}} = R_{\text{cor}}/c$. For a spherical region $\kappa(x, t)$ is given by Eq. (21) of Lightman & Zdziarski (1987).

We compare the results of our numerical model with that from CompPS (Poutanen & Svensson 1996) for a simple Comptonization problem in Appendix A and find good agreement.

4 MODEL SPECTRA

Our model has in total 8 – 11 parameters that control different features of the emergent spectrum:

- (i) $\hat{M}_{\text{BH}} \equiv \alpha M_{\text{BH}}/M_\odot$: Normalized BH mass
- (ii) T_{in} : Disk temperature at the inner disk radius R_{in}
- (iii) \hat{R}_{cor} : Fractional size of the corona in terms of R_{in}
- (iv) ℓ_e/ℓ_d : the ratio of the particle (e^\pm -pairs) compactness to that of the disk radiation, where the latter, $\ell_d \propto \hat{M}_{\text{BH}} T_{\text{in}}^4 / \hat{R}_{\text{cor}}$, depends on the combination of other three parameters
- (v) p : Radial power-law index of the disk temperature
- (vi) f_{out} : Fraction of the comptonized disk radiation intercepted by the outer disk
- (vii) \hat{R}_{out} : Outer disk radius in terms of R_{in}
- (viii) γ_{inj} : Lorentz factor of the e^\pm -pairs injected into the corona when using a δ -function distribution
- (ix) γ_M : Maximum Lorentz factor of the e^\pm -pairs when using a power-law distribution with $\gamma_m = 1$
- (x) s : Power-law index of the injected e^\pm -pairs
- (xi) N_H : Column density of the ISM; in some cases it represents only the extra-Galactic column density

The number of parameters vary depending on whether the particle distribution is a power law or delta-function. Below we show model spectra by varying those model parameters whose effect is non-trivial.

The left column of Fig. 1 shows the effect of varying ℓ_d which can be obtained by varying the three fundamental model parameters, namely \hat{M}_{BH} , T_{in} , \hat{R}_{cor} , as can be seen from Eq. (3); changes in T_{in} would also shift the spectral peak of the disk emission. The νF_ν thermal peak appears approximately at $E_{\text{pk}} \simeq 2.82k_B T_{\text{in}}$, and not exactly at this energy due to some broadening of the peak caused by Comptonization. As the disk radiation compactness ℓ_d is increased, the Comptonized spectrum above the thermal peak becomes harder. Since the Thomson optical depth of pairs in the corona is $\tau_T > 1$, the particle distribution thermalizes at $T_e > T_{\text{in}}$, where T_e is the temperature of the pairs. T_e is sensitive to τ_T and a larger τ_T , which

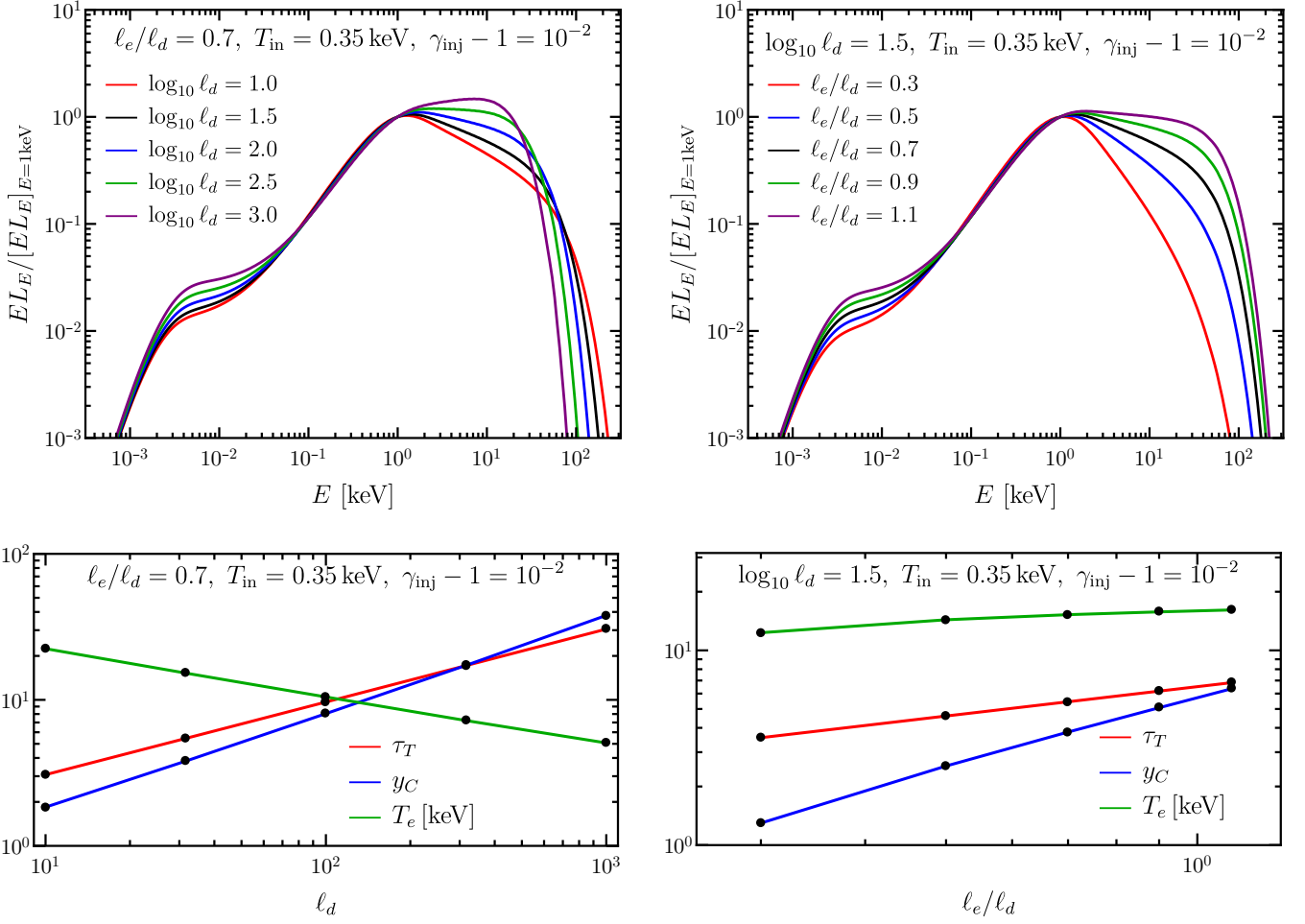


Figure 1. Steady-state model spectra for different disk compactness ℓ_d (top-left; obtained by changing \dot{M}_{BH}), and different compactness ratios ℓ_e/ℓ_d (top-right). The non-relativistic e^\pm -pairs are injected as a delta-function with injection LF γ_{inj} and the disk photons have an MCD spectrum with $p = 0.75$. For clarity all the spectra are normalized by their luminosity at $E = 1$ keV and the pair-annihilation line at $E = 511$ keV has been removed. Other fiducial model parameters assumed here are: $\xi = 0.41$, $\kappa = 1.7$, $f_{\text{out}} = 10^{-2}$, $\hat{R}_{\text{out}} = 5 \times 10^4$, $\hat{R}_{\text{cor}} = 10$.

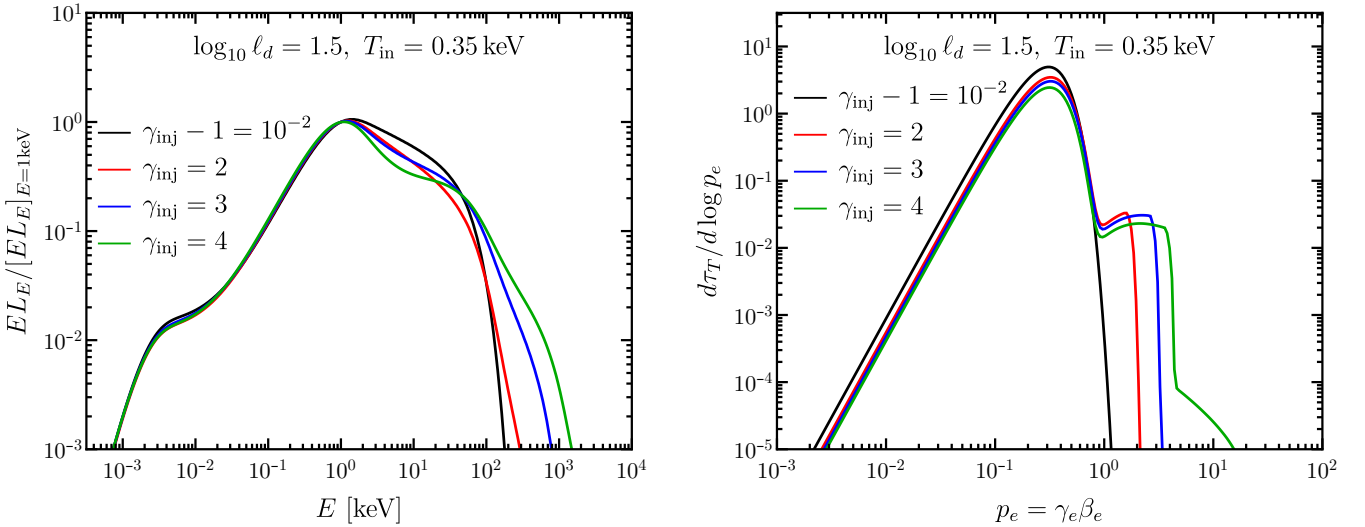


Figure 2. (Left) Steady state model spectra with different γ_{inj} for a δ -function particle injection. (Right) The corresponding steady state particle distribution. All other parameters are the same as in Fig. 1.

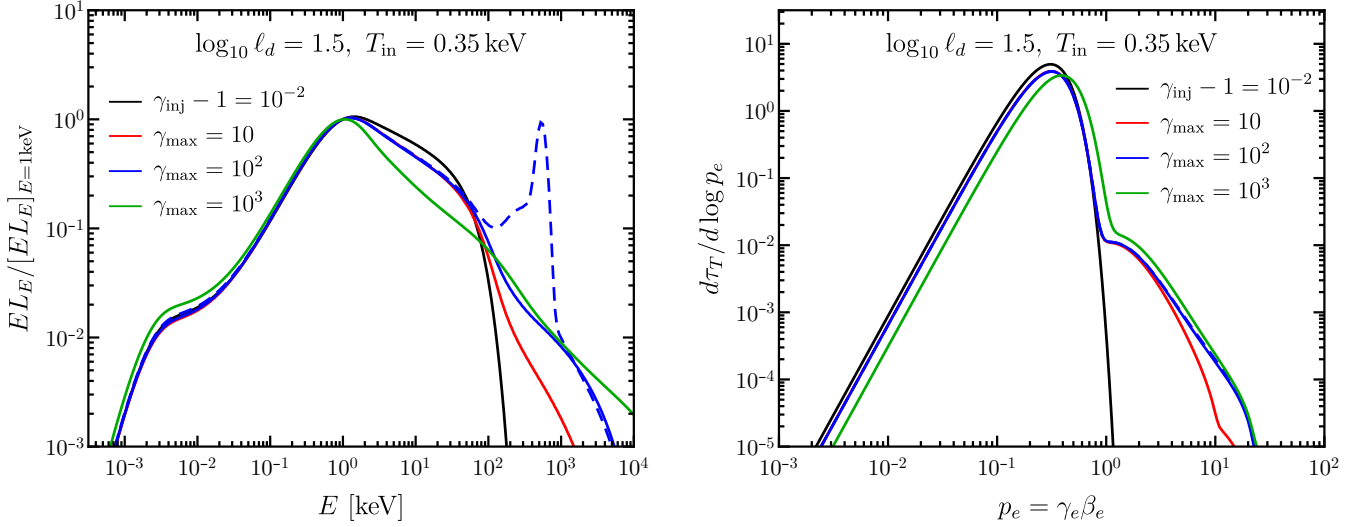


Figure 3. (Left) Steady state model spectra with different γ_{\max} for a power-law particle distribution injection with $\gamma_{\min} = 1$ and power-law index $s = 3.5$. The dashed curve shows the spectrum with contribution from the e^{\pm} -pair annihilation line included. (Right) The corresponding steady state particle distribution. All other parameters are the same as in Fig. 1.

for a fixed \hat{R}_{cor} would mean larger number of particles, would lead to a smaller mean energy per particle and therefore lower T_e . The importance of Comptonization is determined by the Compton- y parameter, $y_C = (4/3)\langle p_e^2 \rangle \max(\tau_T, \tau_T^2)$, where $\langle p_e^2 \rangle = 3\theta_e$ for a non-relativistic Maxwellian, with particle non-dimensional temperature $\theta_e \equiv k_B T_e / m_e c^2 < 1$. We show the trend of τ_T , y_C , and T_e with disk emission compactness ℓ_d in the bottom row of Fig. 1. When $\tau_T \gtrsim 1$ and $y_C \gtrsim 1$, Comptonization proceeds in the unsaturated regime (e.g., Rybicki & Lightman 1986) and the formation of a Wien peak at $E = 3k_B T_e$ is delayed until $y_C \gg 1$ (saturated Comptonization). In the present case, the spectrum shows a power-law above the thermal peak energy and an exponential cutoff (a Wien tail) at $E \approx 3k_B T_e$. Therefore, as τ_T increases due to increasing ℓ_d , the particle temperature declines and the exponential cutoff accordingly moves to lower energies while the spectrum becomes harder due to the rising y_C .

The effect of varying the compactness ratio ℓ_e / ℓ_d is demonstrated in the right column of Fig. 1 for a fixed ℓ_d with the same rest of the parameters. The spectral trend is similar to that shown in the top-left panel, however, with one important difference. In this case, as can be seen from the bottom-right panel, the temperature remains approximately steady since the change in τ_T is rather modest. Consequently, the exponential break remains at the same energy for different values of ℓ_e / ℓ_d . The spectrum still hardens due to the increasing particle compactness ℓ_e which yields larger y_C .

In both cases, the spectrum remains below the $\gamma\gamma$ pair-creation threshold of $E_{\gamma\gamma} \approx m_e c^2$, and therefore, apart from the injected pairs there is no additional pair creation. Since the pairs remain non-relativistic, with $\theta_e < 1$, they do annihilate. For a warm plasma, the pair-annihilation cross-section can be approximated as $\langle \sigma_{\text{ann}} | \vec{v}_+ - \vec{v}_- \rangle \approx (3/8)\sigma_T c$. This yields the rate of annihilation in terms of the rate of decline in the total optical depth

$$\frac{d\tau_T}{dt} \Big|_{\text{ann}} \approx \frac{3}{16} \frac{\tau_T^2}{(R_{\text{cor}}/c)}, \quad (19)$$

which increases quadratically with increasing optical depth. By comparing the rate of injection from Eq. (17), e.g. for a delta-function injection case, $d\tau_{T,\text{inj}}/dt = 2\sigma_T R_{\text{cor}} dn_{\pm,\text{inj}}/dt$, we can derive the condition for steady-state at which point the injection and

annihilation rates are equal,

$$\begin{aligned} \tau_{T,\text{steady state}} &= \sqrt{\frac{4}{\pi} \frac{\ell_e}{\gamma_{\text{inj}}}} \\ &\approx 0.6 \left[\frac{(\ell_e/\ell_d)}{[\gamma_{\text{inj}} \hat{R}_{\text{cor}}]} \right]^{1/2} \left(\frac{\xi}{0.41} \right)^{-1} \left(\frac{\kappa}{1.7} \right)^{-2} \left(\frac{\hat{M}_{\text{BH}}}{10} \right)^{1/2} \left(\frac{k_B T_{\text{in}}}{0.1 \text{ keV}} \right)^2. \end{aligned} \quad (20)$$

Another common feature in both scenarios is the rising normalization of the irradiated disk component. This occurs due to the fact that L_c/L_d scales positively with both ℓ_d and ℓ_e/ℓ_d , which changes the normalization of the irradiated disk temperature θ_{irr} .

The above equation for $\tau_{T,\text{steady state}}$ cannot be strictly used to constrain the coronal properties in other accreting systems, particularly in active galactic nuclei (AGN), since it neglects the creation of e^{\pm} pairs via $\gamma\gamma$ -annihilation, which would necessarily occur in AGN coronae. However, order of magnitude estimates can still be obtained. For example, the hot coronae of AGNs with electron temperatures $k_B T_e \sim (10 - 500) \text{ keV}$ have optical depths of $\tau_T \sim 0.1 - 4$ (e.g., Fabian et al. 2017; Tortosa et al. 2018). The soft photon (blackbody disk emission) spectrum in these systems have characteristic temperatures of $k_B T_{\text{in}} \sim 5 \text{ eV}$ (e.g., Shang et al. 2005) and the system is typically not so much photon starved with $\ell_e/\ell_d \sim 5$. Then for $\hat{M}_{\text{BH}} = 10^{8.5}$, $\gamma_{\text{inj}} = 10^3$, and $\hat{R}_{\text{cor}} = 1$, we get $\tau_{T,\text{steady state}} = 0.6$, which is consistent with order unity coronal optical depths inferred in AGNs.

The effect of increasing the Lorentz factor γ_{inj} of the injected pairs for a δ -function distribution is shown in Fig. 2. The left panel of the figure compares the injection of relativistic monoenergetic particles with the fiducial case where the injected particles are non-relativistic with $\gamma_{\text{inj}} - 1 = 10^{-2}$. As γ_{inj} is increased the spectrum above the thermal peak becomes softer as the inverse-Compton scattered peak, at $E_C = (4/3)\gamma_{\text{inj}}^2 E_{\text{th}}$, moves to larger energies. A secondary inverse-Compton scattered peak is also visible at higher energies. The right panel of the figure shows the corresponding steady-state particle distribution which remains predominantly thermal due to the large compactness of the thermal disk emission and $\tau_T \gtrsim 1$.

Next, we inject a power-law distribution of particles into the corona with $s = 3.5$ and varying γ_{\max} while keeping $\gamma_{\min} = 1$. The

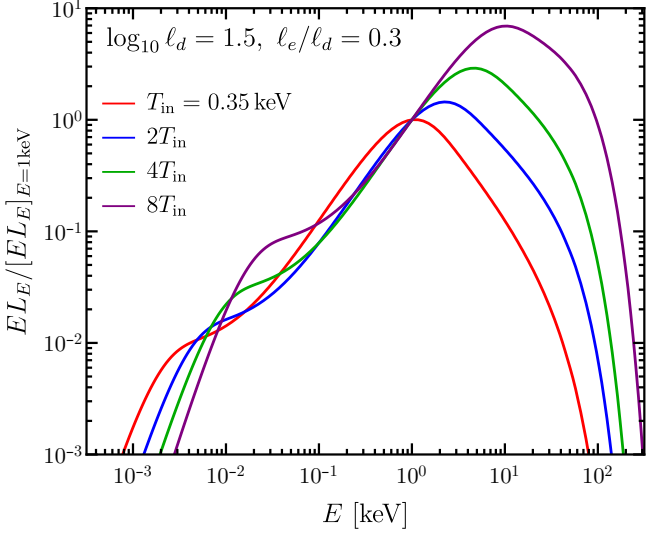


Figure 4. Steady-state model spectra with different inner disk temperature T_{in} , and with $\gamma_{\text{inj}} = 1 + (3/2)\theta_{\text{inj}}$ where $\theta_{\text{inj}} = 10k_B T_{\text{in}}/m_e c^2$. The rest of the parameters, except \dot{M}_{BH} and/or \hat{R}_{cor} , are the same as in Fig. 1. \dot{M}_{BH} and/or \hat{R}_{cor} were changed accordingly in order to keep a fixed ℓ_d .

steady-state spectra and particle distributions are shown in Fig. 3. Even here the spectrum above the thermal peak is softer than the fiducial case (black curve), but it extends to increasingly larger energies as γ_{max} is increased. The high-energy tail is also shaped by $\gamma\gamma$ -annihilation as the spectral luminosity increases above the pair-creation threshold of $\sim m_e c^2$. In all the spectra shown here, we have removed the contribution of the pair annihilation line that appears at $E = 511$ keV. How the spectrum would change if it was included is demonstrated for one of the cases (blue dashed curve). Since there is no particle escape from the corona, e^\pm -pair annihilation acts as a way to remove particles so that a steady state can be obtained. The particle distribution now shows a distinct high-energy tail that constitutes the steady-state distribution of the cooled pairs. This results in a ‘hybrid’ distribution (Coppi 2000) which has both thermal and non-thermal components.

In Fig. 4, we show that as long as the disk and coronal plasma compactness (ℓ_d and ℓ_e) are kept fixed, the steady state spectral shape remains approximately constant, apart from a translation of the spectrum to higher energies as well as towards higher luminosities, both owing to the rising T_{in} . As a result, many of the example model spectra shown for $T_{\text{in}} = 0.35$ keV can be approximately obtained for higher T_{in} with an appropriate shift in the spectral peak energy and normalization. In all the cases shown in Fig. 4 τ_T and the Compton- y parameters are very similar.

The effect of changing the temperature profile of the disk, $\theta(\hat{R}) \propto \hat{R}^{-p}$, with different power-law indices is shown in Fig. 5. A harder temperature profile causes the flux to shift to lower energies thereby softening the spectrum below the thermal peak.

5 HOLMBERG IX X-1: BH MASS ESTIMATES

Holmberg IX X-1 is one of the most widely studied bright ULXs in the last two decades (e.g., La Parola et al. 2001; Wang 2002; Miller et al. 2004; Dewangan et al. 2006; Tsunoda et al. 2006; Gladstone et al. 2009; Kaaret & Feng 2009; Kong et al. 2010; Vier-

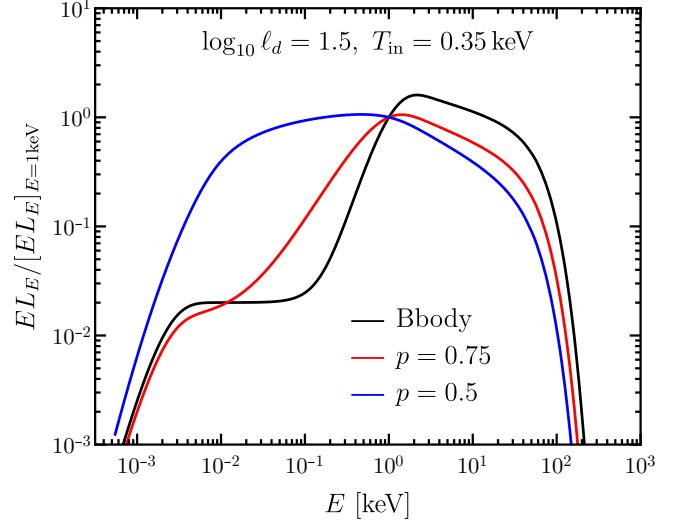


Figure 5. Comparison of steady-state spectra with different temperature profile for the disk, $\theta(\hat{R}) \propto \hat{R}^{-p}$. The multicolor disk spectra are compared with the case of blackbody emission coming from the inner-disk radius. The rest of the parameters are the same as in Fig. 1.

dayanti et al. 2010; Walton et al. 2013, 2014; Luangtip et al. 2016; Walton et al. 2017) owing to its extreme persistent luminosity of $L_X > 10^{40}$ erg s^{-1} . It is associated with the dwarf galaxy Holmberg IX, a satellite of the spiral galaxy M81, at a distance of $D \simeq 3.55$ Mpc. Initial spectral modeling of Holmberg IX X-1, that utilized the XMM-Newton data, revealed a soft, with $k_B T_{\text{in}} \sim (0.17 - 0.29)$ keV, disk component plus power-law continuum that completely dominates the spectrum at $E \gtrsim 2$ keV (Miller et al. 2004). Based on this it was argued that if the ULXs follow the scaling relation, $T_{\text{in}} \propto M_{\text{BH}}^{-1/2}$, as is true for the GBHBs, then Holmberg IX X-1 must harbor a BH with mass $M_{\text{BH}} \sim \text{few} \times 10^2 M_\odot$ if it is accreting at or near L_{Edd} . The IMBH interpretation precludes the presence of spectral curvature in the hard spectrum, which was later discovered in the $\sim 2 - 10$ keV energy band the origin of which was found to be optically-thick ($\tau_T \sim 5 - 30$) coronae (Stobbart et al. 2006; Dewangan et al. 2006; Gladstone et al. 2009; Walton et al. 2013). A disk plus thermal Comptonization model, e.g. compTT (Titarchuk 1994) and EQPAIR (Coppi 2000), was used to successfully describe the curved spectrum of Holmberg IX X-1 where the temperature of the Comptonizing corona was found to be $kT_e \sim (2 - 3)$ keV. When NuSTAR data became available for this source, the hard excess above 10 keV was modeled using the SIMPL Comptonization or CUTTOFFPL models (Walton et al. 2014; Luangtip et al. 2016; Walton et al. 2017, 2018).

In the following, we first describe the observations and data reduction procedures for the three different spectra of Holmberg IX X-1 dubbed LOW, MEDIUM, and HIGH based on their relative X-ray fluxes. After that we present the spectral analysis and fit results.

5.1 Observations and Data Reduction

As part of our study of the spectral variability of Holmberg IX X-1, we have analyzed (following Walton et al. 2014) coordinated broadband X-ray NuSTAR, XMM-Newton, and Suzaku observations for 3 epochs spanning the period 2012-2015. For the analysis, we deployed the most up-to-date calibration files for all the instruments.

We note that the Galactic absorption component was removed from all low-energy data by using the responses for each detector. Below, we outline our data reduction procedures for these observations.

5.1.1 XMM-Newton

The XMM-Newton data for the first two epochs (i.e., high flux and medium flux; ObsIDs 0693851701 and 0693850901 respectively) were reduced, and source and background spectra, as well as, their redistribution matrices and auxiliary response files (RMF and ARF) were created using the remote interface SAS analysis tool RISA for EPIC-pn and EPIC-MOS detectors. We deployed the pattern 0-4 for pn, and 0-12. for the MOS. To avoid pixels close to CCD boundaries and dead columns FLAG was set to 0. The source spectra were extracted using a circular radius of $\sim 30''$ and care was taken to avoid chip gaps. In all cases the background was extracted using a larger area of the same CCD frame but in a region free from point sources. Finally, the spectra were rebinned using the grppha task in HEASOFT to have a minimum of 50 counts per bin.

5.1.2 Suzaku

We followed the procedure outlined in the Suzaku data-analysis guide¹ to reduce the epoch 4 data by using HEASOFT v2.26.2 for the front illuminated XIS0 and XIS3 units over the 0.6 – 10.0 keV range and XIS1 unit over the 0.7 – 9.0 keV range respectively. Following Walton et al. 2014, we excluded the 1.7 – 2.1 keV range in all three detectors so as to avoid known calibration issues around the instrumental edges. The source spectra were extracted using a circular radius of $\sim 70''$ and a larger source-free region was used to extract the background. All spectra were extracted from cleaned event files using XSELECT. All XIS spectra were rebinned using the grppha task in HEASOFT to have a minimum of 50 counts per bin.

5.1.3 NuSTAR

Corresponding NuSTAR observations (ObsIDs 30002033006, 30002033002, 30002034004) for each epoch were reduced using the standard pipeline NUSTARDAS included in the HEASOFT v2.26.2. Source spectra were created using a circular region with a radius of $\sim 70''$ and the corresponding background was estimated from a larger source-free region of the same detector. All products were extracted from the cleaned event files using XSELECT. Again, the spectra were rebinned to have minimum of 50 counts per bin. The NuSTAR spectra used in this work are modeled over the 3.0–30 keV range.

5.1.4 HST

Holmberg IX X-1 has been reported as one of the ULXs with a unique optical counterpart (Kaaret et al. 2004; Tao et al. 2011; Gladstone et al. 2013). In this work, the intrinsic vega magnitudes were taken directly from Dudik et al. (2016) where they presented the multi-band photometric properties from the analysis of archival imaging data taken by the Hubble Space Telescope (HST). A summary of archival HST data used for the analysis is presented in Table 1.

¹ <http://heasarc.gsfc.nasa.gov/docs/suzaku/analysis/>

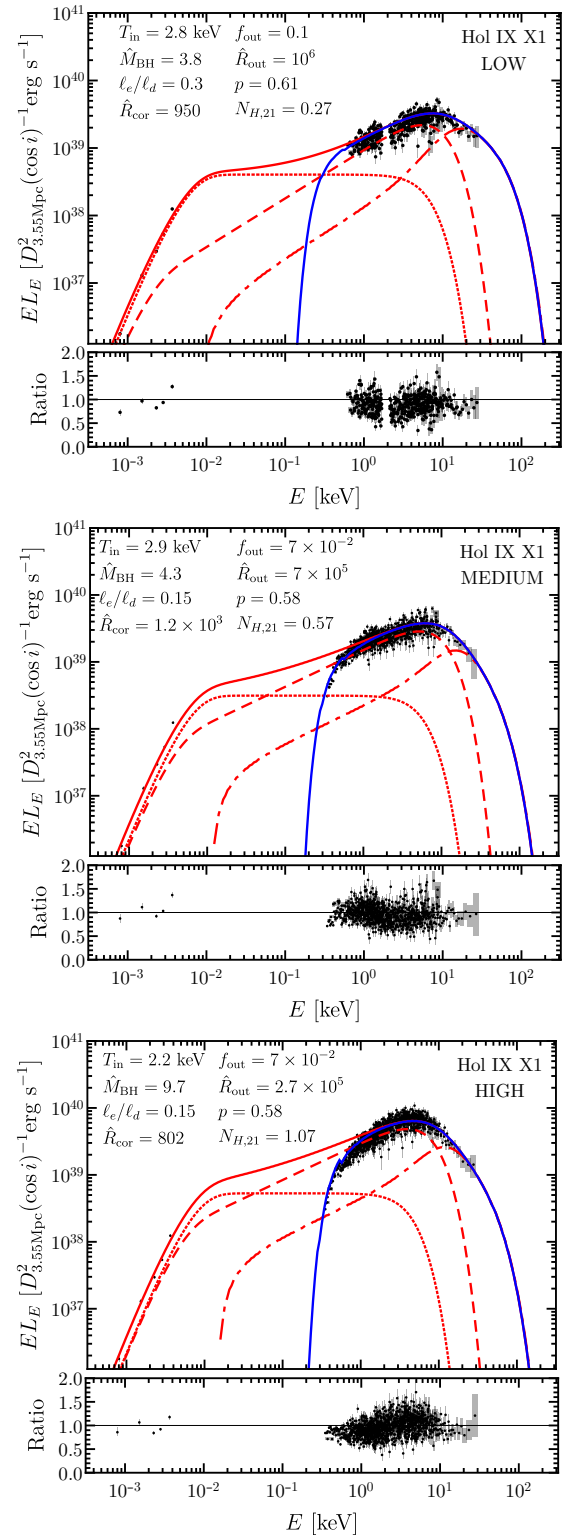


Figure 6. Two-component disk-corona model fit to the broadband spectrum of Holmberg IX X-1, shown for three different spectral states (corresponding to the relative level of flux) dubbed HIGH, MEDIUM, and LOW. The data has been corrected for Galactic absorption. The solid red curve shows the de-absorbed best-fit spectrum obtained with non-linear least squares and the dashed, dot-dashed, and dotted red curves show the multi-color disk, Comptonized, and irradiated disk spectral components, respectively. The spectrum modified by absorption local to the source is shown by the blue curve. Bottom panel shows the data/model ratio. In all cases, the steady-state corona is optically thick with fit results given in Table 3.

Instrument	Obs ID	Filter	Obs. Date	Flux density μJy	Abs. A_λ	Corrected μJy
Hubble ACS	GO-9796	F814W/I	2004 Feb 7	2.99±0.19	0.47	4.67±0.29
Hubble ACS	GO-9796	F555W/V	2004 Feb 7	3.29±0.15	0.81	7.06±0.31
Hubble ACS	GO-9796	F435W/B	2004 Feb 7	3.87±0.10	1.08	10.4±0.29
Hubble ACS	GO-9796	F330W/U	2004 Feb 7	5.47±0.23	1.33	18.6±0.74
Hubble WFC3/IR	GO-12747	F160W/H	2012 Sep 25	1.01±0.09	0.202	1.21±0.12

Table 1. A summary of archival HST data (reproduced from Dudik et al. (2016))

Model Parameters From MCMC						
Spectral State	$k_B T_{\text{in}}$ (keV)	\hat{M}_{BH}	ℓ_e/ℓ_d	$\log_{10} \hat{R}_{\text{cor}}$	p	$N_{H,21}$
LOW	2.75 ^{+0.59} _{-0.61}	3.91 ^{+0.58} _{-0.29}	0.20 ^{+0.19} _{-0.13}	2.99 ^{+0.40} _{-0.45}	0.62 ^{+0.10} _{-0.09}	0.15 ^{+0.37} _{-0.11}
MEDIUM	2.99 ^{+0.54} _{-0.35}	4.36 ^{+1.71} _{-1.52}	0.20 ^{+0.22} _{-0.13}	3.00 ^{+0.68} _{-0.72}	0.63 ^{+0.09} _{-0.11}	0.66 ^{+0.78} _{-0.38}
HIGH	2.24 ^{+1.09} _{-0.83}	9.68 ^{+0.33} _{-0.60}	0.23 ^{+0.19} _{-0.16}	2.98 ^{+0.61} _{-0.59}	0.60 ^{+0.11} _{-0.07}	1.18 ^{+0.38} _{-0.56}

Table 2. Fit parameters and corresponding 1- σ uncertainties obtained from the MCMC simulation.

Spectral State	Best-Fit Model Parameters (8)							Steady-State Corona Properties (4)				
	$k_B T_{\text{in}}$ (keV)	\hat{M}_{BH}	ℓ_e/ℓ_d	\hat{R}_{cor}	p	$N_{H,21}$	f_{out}	$\hat{R}_{\text{out},5}$	$k_B T_e$ (keV)	τ_T	γ_C	L_c/L_d
LOW	2.8	3.81	0.3	950	0.61	0.27	0.1	10.0	15.5	4.4	2.4	0.94
MEDIUM	2.9	4.3	0.15	1198	0.58	0.57	0.07	7.0	13.3	3.1	1.1	0.47
HIGH	2.2	9.7	0.15	802	0.58	1.07	0.07	2.7	12.6	3.3	1.1	0.47

	$L_{\text{Bol}}[\text{erg s}^{-1}]$	$L_{(0.3-10)\text{keV}}[\text{erg s}^{-1}]$	χ^2/dof
LOW	1.1×10^{40}	6.9×10^{39}	1937/433
MEDIUM	1.2×10^{40}	8.4×10^{39}	4066/820
HIGH	2.4×10^{40}	1.6×10^{40}	4308/970

Table 3. Best fit parameters obtained with non-linear least squares for the three spectral states. There are eight model parameters. The steady state description of the e^\pm -pair corona is given by the four parameters that were obtained at the end of the simulation. The bolometric and (0.3 – 10) keV luminosities for the three spectral states are also listed. Here we use the notation where Q_x denotes the quantity Q in units of 10^x times its (cgs) units.

5.2 Spectral Analysis: BH Mass Fits

We use the two-component multi-color disk-corona spectral model to fit the broadband spectrum of Holmberg IX X-1. The fits were first carried out using Markov Chain Monte Carlo (MCMC) simulations to obtain the most probable model parameters and their corresponding 1- σ uncertainties. The results of the MCMC simulation are tabulated in Table 2 and the posterior probability distributions of the model parameters are shown in Appendix B. The best-fit model parameters were obtained from a least-squares fit and they are tabulated in Table 3 and the fits to the spectra are shown in Fig. 6.

We find significant local absorption with $N_H \sim (0.3 - 1.0) \times 10^{21} \text{cm}^{-2}$, which is a factor $\sim (0.4 - 1.2)$ of the Galactic absorption in the direction of Holmberg IX X-1. The measurements presented in Fig. 6 are corrected for the Galactic absorption that contributes a column density of $N_H = 0.813 \times 10^{21} \text{cm}^{-2}$. The amount of absorption caused by material external to our Galaxy is consistent with that found in other works (e.g., Walton et al. 2014; Luangtip et al. 2016; Walton et al. 2017). The absorbed spectrum is shown with a blue line, for which we use the absorption cross-section of Wilms et al. (2000) (see their Fig. 1), and the de-absorbed spectrum is shown with a red line.

The best-fit solutions presented in Fig. 6 for the three different spectral states describe an accreting system where the mass of the

accretor is $4 \lesssim \hat{M}_{\text{BH}} \lesssim 10$ and the inner disk temperature is consistently high with $2 \text{keV} \lesssim k_B T_{\text{in}} \lesssim 3 \text{keV}$. Both of these parameters determine the normalization of the spectrum originating in the disk as well as the properties of the Comptonized spectral component. It is understood that \hat{M}_{BH} cannot change in between different spectral states and must remain constant. In the spectral fits it was left as a free parameter so as not to bias it towards any given solution. Instead, it is clear that \hat{M}_{BH} is indeed constrained in a narrow range and all spectral states are explained by a stellar mass BH accretor. The inner disk temperature obtained here is consistent with that found by other works (e.g., Luangtip et al. 2016; Walton et al. 2017, 2018) that modeled the spectrum using two thermal spectral components, namely a combination of DISKBB and DISKPBB models. The DISKPBB component was always found to be hotter of the two and that is what the MCD spectral component (dashed curve) shown in Fig. 6 represents.

The hard excess above 10 keV, as revealed by *NuSTAR*, is explained here by the Comptonized emission (dash-dotted curve) originating in the corona. In empirical model spectral fits this component is typically explained using a CUTOFFPL or SIMPL model. We obtain the Comptonized emission by injecting into the corona a non-relativistic and monoenergetic e^\pm -pair distribution with $\gamma_{\text{inj}} = 1.1$ that corresponds to an effective temperature of $k_B T_{\text{eff}} = (2/3)(\langle\gamma_e\rangle - 1)m_e c^2 \approx 34 \text{keV}$. Even though the pairs are being continuously in-

jected at this temperature, the mean temperature of the pair distribution in the corona declines rapidly due to the large compactness ($\ell_d \sim 60$) of the disk emission that Compton cools the pairs to a lower temperature as the system approaches a steady state. The steady state distribution of pairs is a Maxwellian with temperature in the range $k_B T_e \sim (12 - 15)$ keV and the Thomson optical depth of the corona is modest ($\tau_T \sim 3.5$). The Compton- y parameter of the coronal plasma is of order unity and the system never reaches the stage where saturated Comptonization would establish a pronounced Wien peak at $E = 3k_B T_e$, the energy beyond which the model spectrum would drop off exponentially.

When comparing the model parameters for the three states, the inner disk temperature, T_{in} , shows a small spread which explains the narrow spread in the spectral peak energy. Since the disk luminosity scales as $L_d \propto T_{in}^4$, even a small change in the inner disk temperature can bring a large change in the normalization of the peak luminosity. However, the trend appears to be reversed when comparing the MEDIUM and HIGH spectral fits, where T_{in} is larger in the MEDIUM spectral state. The rise in flux density in the HIGH state is accounted for by the larger value for \hat{M}_{BH} . This negative trend between disk luminosity and inner disk temperature was also noted by Luangtip et al. (2016). Indeed, it finds a natural explanation in super-critical accretion models (see, e.g., extensive discussion in Luangtip et al. 2016; Walton et al. 2017).

The disk temperature profile power law index remains almost constant, with $p \approx 0.6$, among all the spectral states. This result is also consistent with other works (e.g., Walton et al. 2017).

The properties of the coronal plasma are rather uniform among the three states, which is indicative of the fact that it is mainly the disk emission that is changing. The coronal plasma is not photon starved (i.e. $\ell_e/\ell_d < 1$) which explains why the steady state particle temperature (~ 14 keV) is lower than their injection temperature (34 keV), where the particles have been cooled due to Comptonization. The size of the corona also remains more or less constant between the different flux states, with $\hat{R}_{cor} \sim 10^3$.

A large spread is seen in the value of the absorption column density local to the source. This affects the degree of X-ray flux suppression at energies $\lesssim 2$ keV, which appears to be significant for the HIGH state. Since there is insufficient data below 0.5 keV for the LOW state, the inferred value of the column density cannot be trusted. This is also clear from the MCMC fit shown in Fig. B1 where a distinct peak in the posterior distribution away from the boundary values is missing.

To constrain the size of the disk and the disk irradiation physics we have included archival HST observations and carried out broadband spectral fits. These observations are not contemporaneous with the X-ray observations and so do not probe the effect of spectral states on the inferred disk irradiation model parameters directly. However, such an exercise does demonstrate the potential of fitting contemporaneous broadband observations with our model. The inferred values of the two parameters $f_{out} \sim 0.08$ and $\hat{R}_{out} \sim 7 \times 10^5$ are consistent with other works that fit broadband optical/UV and X-ray data of ULXs (e.g., Gierliński et al. 2009; Sutton et al. 2014). The irradiated disk model fit to the HST data depends on the model fits to the X-ray data but not vice versa. Therefore, even though the HST observations included here are not contemporaneous, these do not affect the other six model parameters, including \hat{M}_{BH} , that rely solely on the X-ray data. This is the reason behind not including the HST data in the MCMC fits. Furthermore, due to insufficient UV data that would constrain the spectral break, the irradiated disk model is degenerate in the two parameters and as such f_{out} and \hat{R}_{out}

cannot be constrained well. Therefore, the obtained irradiated disk parameters are not unique.

6 DISCUSSION

In this work we have tried to understand the origin of what appears to be a three-component X-ray spectrum of ULXs in the (0.3 – 30) keV band using a physical model that features a multi-color disk plus Comptonizing corona. Here the inner accretion disk contributes a MCD thermal spectrum that describes the X-ray spectrum below 10 keV whereas a hotter corona of e^\pm -pairs Comptonizes the disk radiation to give the high-energy component above 10 keV. We have used a time-dependent kinetic code to evolve the coupled leptophotonic equations of radiation transfer to obtain the two-component X-ray spectrum. In addition, we self-consistently produce the irradiated disk-component that explains the low-energy optical/UV spectrum of ULXs.

The prime motivations behind this work were to (i) explain as self-consistently as possible the origin of the X-ray spectrum and (ii) constrain the mass of the central compact object – a major open question, which is in fact one of the parameters of our model. Here we apply our spectral model to fit to the different spectral states of one of the most well studied and luminous ULXs, Holmberg IX X-1, and constrain the mass of the accretor. Our working assumption is that the accretor is a BH and we constrain its mass to be in the range $4 \lesssim \hat{M}_{BH} \lesssim 10$. Here $\hat{M}_{BH} \equiv \alpha M_{BH}/M_\odot$ which depends on the BH spin and therefore the mass only goes up for a spinning BH for which $1/6 \leq \alpha < 1$. The normalization of the MCD component scales as $L_d \propto M_{BH}^2 T_{in}^4$, and therefore a lower \hat{M}_{BH} naturally means a higher inner disk temperature T_{in} and vice versa. In addition, since the luminosity changes with source distance and inclination, such that $L \propto D^2/\cos i$, Eq. (2) yields the scaling $M_{BH} \propto D/\sqrt{\cos i}$. Therefore, a larger distance or larger inclination angle would tend to increase the \hat{M}_{BH} estimate. A similar change results in \hat{R}_{cor} when T_{in} can be fixed since $\ell_d \propto \hat{M}_{BH}/\hat{R}_{cor}$ (when $\hat{R}_{cor} > 1$) and to obtain the same spectrum, albeit with a different overall normalization, ℓ_d must remain unchanged.

Previous BH mass estimates in Holmberg IX X-1 have ranged from $(10 - 10^3)M_\odot$ based on spectral modeling (e.g., Wang 2002; Miller et al. 2003; Kong et al. 2010) and $(50 - 200)M_\odot$ from the detection of quasi-periodic oscillations (QPOs; Dewangan et al. 2006). In general, mass estimates in ULXs have relied on a few different methods (Miller et al. 2003, 2004, 2013). For example, the standard thin-disk scaling relation $T_{in} \propto M_{BH}^{-1/4}$ is often employed with the underlying assumption that ULXs are scaled up versions of known accreting sources. Noting that $k_B T_{in,GBHB} \sim 1$ keV in Galactic BHBs, that are powered by stellar-mass BHs with $M_{BH} \sim 10M_\odot$, as compared to $k_B T_{in,ULX} \sim 0.1 - 0.3$ keV, the temperature of the cooler thermal disk emission, this yields $M_{ULX} \sim 10^3 - 10^5 M_\odot$. Accordingly, the higher disk temperatures obtained from the spectral fits in this work are commensurate with having a stellar mass BH in Holmberg IX X-1. Alternatively, when using the MCD model a more direct mass estimate is possible where the normalization of the disk luminosity depends on M_{BH} . This of course makes the assumption that the disk extends all the way to R_{ISCO} . Indeed, having made the same assumptions in this work, we were able to constrain M_{BH} directly as it is one of the model parameters. Another useful way of constraining the mass is by comparing the bolometric luminosity with L_{Edd} assuming an accretion efficiency $\eta \equiv L_{Bol}/L_{Edd} < 1$. Having determined the masses using an independent method, we can use L_{Edd} to constrain η . For the obtained mass range the Eddington luminosity is

$L_{\text{Edd}} \simeq (0.5 - 1.3) \times 10^{39} \alpha^{-1} \text{ erg s}^{-1}$. By comparing it with the bolometric luminosities obtained for the three flux states, we find that $\eta \sim 20\alpha$, which indicates super-critical accretion.

While low ($k_B T_{\text{in}} \sim 0.1 - 0.3 \text{ keV}$) disk temperatures are the hallmark of ULXs, some works do find high ($k_B T_{\text{in}} \gtrsim 1 \text{ keV}$) disk temperatures, particularly for the highly luminous states, when fitting in many cases with dual thermal models that feature either two MCD or MCD plus blackbody components (Stobart et al. 2006; Walton et al. 2014; Luangtip et al. 2016; Walton et al. 2017). As argued above, in the standard thin-accretion disk models lower T_{in} necessarily yields $M_{\text{BH}} > 100M_{\odot}$, one promising way to obtain lower BH masses is by having higher T_{in} . In that case, we find that as T_{in} is raised, moving the thermal peak to higher energies, the spectral slope below the peak cannot be explained with the disk temperature profile having power-law index $p = 0.75$. Instead, the temperature profile must deviate from the standard thin-disk relation and must be harder with $p \sim 0.6$, a result consistent with other works (e.g. Walton et al. 2014, 2017). Such a change might be indicative of radiation pressure effects operating in the hot inner disk, as would be obtained in super-critical accretion, which would alter the temperature profile, as in a slim accretion disk (e.g. Abramowicz et al. 1988; Poutanen et al. 2007).

The spectral model employed in this work has only two components in the X-ray band (the third component being the irradiated disk component that appears only in the optical/UV energy band), in contrast to many works that use two spectral components to fit the softer X-ray emission below $\sim 10 \text{ keV}$ and an additional component to fit the hard excess revealed by *NuSTAR* above $\sim 10 \text{ keV}$. As such, we only model the hotter of the two thermal components with an MCD for the softer X-ray emission. The harder excess in our model is given by the Comptonized emission, which is typically modeled using a CUTOFFPL or SIMPL empirical model in many works. Although the cooler of the two thermal components contributing to the softer X-ray emission is found to be subdominant (e.g., Luangtip et al. 2016; Walton et al. 2017), its inclusion is statistically demanded. The lack of such a component in the present work leads to some structure in the data/model ratios, as shown in Fig. 6, and produces rather high values of the χ^2 fit statistic.

Many works model the hotter thermal component as Comptonized emission by thermal electrons using either COMPTT or EQPAIR models (e.g., Stobart et al. 2006; Gladstone et al. 2009; Luangtip et al. 2016). In such a case the softer thermal component would be the MCD emission. When we try to model the X-ray spectrum of Holmberg IX X-1 with our model in this manner, we find that a lower T_{in} can only be accommodated if $\hat{R}_{\text{cor}} \ll 1$. This further implies that the solid angle offered by the corona is rather small and most of the disk emission is not intercepted. Therefore, the Comptonized emission should be sub-dominant and ultimately inadequate to explain the X-ray spectrum at energies beyond $\sim 1 \text{ keV}$. As a result, the cooler of the two thermal components, when statistically required, must have a different origin in our model. Its origin and significance will be investigated in future works.

The hotter thermal component finds a natural explanation in models featuring super-critical accretion with massive outflowing winds (Abramowicz et al. 1988; Poutanen et al. 2007; King 2009; Dotan & Shaviv 2011; Ohsuga & Mineshige 2011; Takeuchi et al. 2013). Radiation pressure effects lead to large scale heights of the disk and massive winds that are shaped into a funnel geometry around the rotational axis of the compact source. The softer thermal component then emerges as photospheric emission from the walls of this funnel while the hotter component has its origin in the inner regions of the accretion flow. Then, for a given line-of-sight the different spectral

states can occur due to changes in the accretion rate which would alter the scale height, and correspondingly the position of the funnel wall, of the accretion disk (Middleton et al. 2015). Alternatively, if the accretion disk precesses, that too can lead to spectral changes due to the change in the inclination angle of the line-of-sight (e.g. Luangtip et al. 2016).

In this work, we have also attempted to self-consistently explain the optical/UV emission using the irradiated disk model (Gierliński et al. 2009). The self-consistency comes from obtaining the ratio L_c/L_d from the steady state solution. The value of this parameter is usually assumed a priori in all works. When the optical/UV data is missing the spectral break or shoulder (around $\sim 10 \text{ eV}$), as was the case in the archival HST data used here, the two parameters, \hat{f}_{out} and \hat{R}_{out} , become degenerate that precludes obtaining strong constraints. Future nearly contemporaneous observations by, e.g. *Swift/UVOT* and *XRT*, where the former might be able to localize the spectral break in some sources, with *NuSTAR* are encouraged.

6.1 Caveats: Super-Critical Accretion

As shown earlier, for the narrow range of BH masses obtained in this work, we find accretion to be proceeding in the super-critical regime in Holmberg IX X-1. This naturally questions the validity of using a p -free thin accretion disk formalism, as the emission might be arising from or significantly modified by massive radiative winds that produce flux enhancements due to geometric beaming and also impose inclination angle dependent spectral variations. The bolometric isotropic-equivalent luminosity of a super-critically accreting BH is (Begelman et al. 2006; Poutanen et al. 2007; King 2009)

$$L_{\text{Sph}} \simeq L_{\text{Edd}} \frac{(1 + \ln \dot{m})}{b} = 2L_d \simeq 2\eta L_{\text{Edd}}, \quad (21)$$

where $\dot{m} = \dot{M}/\dot{M}_{\text{Edd}}$ is the Eddington normalized mass accretion rate and b is the geometric beaming factor. For $\eta \sim 20$ and if $b \gtrsim 0.1$ then this yields $\dot{m} \gtrsim 20$. If geometric beaming is indeed important in Holmberg IX X-1, then the intrinsic flux normalization is lower by a factor of $0.1 \lesssim b \lesssim 1$, which implies that the true \dot{M}_{BH} might be smaller by a factor of $0.3 \lesssim \sqrt{b} \lesssim 1$.

In addition, the one-zone model used in this work is incapable of addressing the radiation transfer physics and accounting for the flow geometry. Indeed, this is a limitation of our model and caveat for the obtained results. In order to account for the different effects in such a scenario, a more sophisticated radiation transfer model (e.g. Kawashima et al. 2012) that also accounts for spectral changes due to different inclinations is more appropriate.

The complex geometry of the outflow may also affect the disk irradiation physics. In a sub-Eddington system, which lacks such outflows, the corona irradiates the outer disk directly. In contrast, the massive outflows in a super-critical system are optically thick at large inclinations, and as a result, the coronal emission may be highly suppressed. Therefore, a proper radiation transfer treatment is again required to fully understand these effects.

7 CONCLUSIONS

Our broadband spectral modeling, using a self-consistent two-component MCD plus Comptonizing corona model for the X-ray emission, suggests that Holmberg IX X-1 harbors a stellar mass BH with mass $4 \lesssim \hat{M}_{\text{BH}} \lesssim 10$. With the discovery of pulsations in at least six ULXs, the consensus has now shifted to most of these systems likely hosting accreting NSs and in some cases stellar

mass BHs. No pulsations have been detected from Holmberg IX X-1 thus far, which does favor the conclusions reached in this work. However, non-detection of pulsations is not a sufficient condition to rule out a NS host. Finally, this work demonstrates the use of physical models to arrive at more self-consistent spectral fit solutions. It is envisaged that this technique, when applied to a larger sample of ULXs, will yield important clues to their nature.

ACKNOWLEDGEMENTS

We are grateful to the anonymous referee for several valuable comments that significantly improved the quality of this work. RG is supported by the ISF-NSFC joint research program (grant No. 3296/19). This research is supported by the Scientific and Technological Research Council of Turkey (TUBITAK) through project number 119F334.

DATA AVAILABILITY

The data underlying this article will be shared on reasonable request to the corresponding author.

REFERENCES

- Abramowicz M. A., Czerny B., Lasota J. P., Szuszkiewicz E., 1988, *ApJ*, **332**, 646
- Bachetti M., et al., 2013, *ApJ*, **778**, 163
- Bachetti M., et al., 2014, *Nature*, **514**, 202
- Begelman M. C., 2002, *ApJ*, **568**, L97
- Begelman M. C., King A. R., Pringle J. E., 2006, *MNRAS*, **370**, 399
- Belmont R., 2009, *A&A*, **506**, 589
- Belmont R., Malzac J., Marcowith A., 2008, *A&A*, **491**, 617
- Carpano S., Haberl F., Maitra C., Vasilopoulos G., 2018, *MNRAS*, **476**, L45
- Colbert E. J. M., Mushotzky R. F., 1999, *ApJ*, **519**, 89
- Coppi P. S., 2000, in *AAS/High Energy Astrophysics Division #5*. p. 23.11
- Cropper M., Soria R., Mushotzky R. F., Wu K., Markwardt C. B., Pakull M., 2004, *MNRAS*, **349**, 39
- Dewangan G. C., Griffiths R. E., Rao A. R., 2006, *ApJ*, **641**, L125
- Dotan C., Shaviv N. J., 2011, *MNRAS*, **413**, 1623
- Dudik R. P., Berghea C. T., Roberts T. P., Grisé F., Singh A., Pagano R., Winter L. M., 2016, *ApJ*, **831**, 88
- Fabian A. C., Ward M. J., 1993, *MNRAS*, **263**, L51
- Fabian A. C., Lohfink A., Belmont R., Malzac J., Coppi P., 2017, *MNRAS*, **467**, 2566
- Farrell S. A., Webb N. A., Barret D., Godet O., Rodrigues J. M., 2009, *Nature*, **460**, 73
- Feng H., Kaaret P., 2005, *ApJ*, **633**, 1052
- Feng H., Soria R., 2011, *New Astron. Rev.*, **55**, 166
- Feng H., Tao L., Kaaret P., Grisé F., 2016, *ApJ*, **831**, 117
- Fürst F., et al., 2016, *ApJ*, **831**, L14
- Gierliński M., Zdziarski A. A., Poutanen J., Coppi P. S., Ebisawa K., Johnson W. N., 1999, *MNRAS*, **309**, 496
- Gierliński M., Done C., Page K., 2009, *MNRAS*, **392**, 1106
- Gill R., Thompson C., 2014, *ApJ*, **796**, 81
- Gladstone J. C., Roberts T. P., Done C., 2009, *MNRAS*, **397**, 1836
- Gladstone J. C., Copperwheat C., Heinke C. O., Roberts T. P., Cartwright T. F., Levan A. J., Goad M. R., 2013, *ApJS*, **206**, 14
- Guilbert P. W., Fabian A. C., Rees M. J., 1983, *MNRAS*, **205**, 593
- Israel G. L., et al., 2017a, *Science*, **355**, 817
- Israel G. L., et al., 2017b, *MNRAS*, **466**, L48
- Kaaret P., Feng H., 2009, *ApJ*, **702**, 1679
- Kaaret P., Corbel S., Prestwich A. H., Zezas A., 2003, *Science*, **299**, 365
- Kaaret P., Ward M. J., Zezas A., 2004, *MNRAS*, **351**, L83
- Kaaret P., Feng H., Roberts T. P., 2017, *ARA&A*, **55**, 303
- Kawashima T., Ohsuga K., Mineshige S., Yoshida T., Heinzeller D., Matsumoto R., 2012, *ApJ*, **752**, 18
- King A. R., 2004, *MNRAS*, **347**, L18
- King A. R., 2009, *MNRAS*, **393**, L41
- Koliopanos F., Vasilopoulos G., Godet O., Bachetti M., Webb N. A., Barret D., 2017, *A&A*, **608**, A47
- Kong A. K. H., Yang Y. J., Yen T. C., Feng H., Kaaret P., 2010, *ApJ*, **722**, 1816
- Kubota A., Tanaka Y., Makishima K., Ueda Y., Dotani T., Inoue H., Yamaoka K., 1998, *PASJ*, **50**, 667
- La Parola V., Peres G., Fabbiano G., Kim D. W., Bocchino F., 2001, *ApJ*, **556**, 47
- Lightman A. P., Zdziarski A. A., 1987, *ApJ*, **319**, 643
- Luangtip W., Roberts T. P., Done C., 2016, *MNRAS*, **460**, 4417
- Makishima K., et al., 2000, *ApJ*, **535**, 632
- Merloni A., Fabian A. C., Ross R. R., 2000, *MNRAS*, **313**, 193
- Middleton M. J., Heil L., Pintore F., Walton D. J., Roberts T. P., 2015, *MNRAS*, **447**, 3243
- Miller M. C., Colbert E. J. M., 2004, *International Journal of Modern Physics D*, **13**, 1
- Miller J. M., Fabbiano G., Miller M. C., Fabian A. C., 2003, *ApJ*, **585**, L37
- Miller J. M., Fabian A. C., Miller M. C., 2004, *ApJ*, **607**, 931
- Miller J. M., Walton D. J., King A. L., Reynolds M. T., Fabian A. C., Miller M. C., Reis R. C., 2013, *ApJ*, **776**, L36
- Mineshige S., Hirano A., Kitamoto S., Yamada T. T., Fukue J., 1994, *ApJ*, **426**, 308
- Mitsuda K., et al., 1984, *PASJ*, **36**, 741
- Moon D.-S., Harrison F. A., Cenko S. B., Shariff J. A., 2011, *ApJ*, **731**, L32
- Mukherjee E. S., et al., 2015, *ApJ*, **808**, 64
- Ohsuga K., Mineshige S., 2011, *ApJ*, **736**, 2
- Pintore F., Zampieri L., Stella L., Wolter A., Mereghetti S., Israel G. L., 2017, *ApJ*, **836**, 113
- Poutanen J., Svensson R., 1996, *ApJ*, **470**, 249
- Poutanen J., Lipunova G., Fabrika S., Butkevich A. G., Abolmasov P., 2007, *MNRAS*, **377**, 1187
- Remillard R. A., McClintock J. E., 2006, *ARA&A*, **44**, 49
- Rodríguez Castillo G. A., et al., 2020, *ApJ*, **895**, 60
- Rybicki G. B., Lightman A. P., 1986, *Radiative Processes in Astrophysics*
- Sathyaprakash R., et al., 2019, *MNRAS*, **488**, L35
- Shakura N. I., Sunyaev R. A., 1973, *A&A*, **500**, 33
- Shang Z., et al., 2005, *ApJ*, **619**, 41
- Shimura T., Takahara F., 1995, *ApJ*, **445**, 780
- Steiner J. F., Narayan R., McClintock J. E., Ebisawa K., 2009, *PASP*, **121**, 1279
- Stobart A. M., Roberts T. P., Wilms J., 2006, *MNRAS*, **368**, 397
- Sutton A. D., Done C., Roberts T. P., 2014, *MNRAS*, **444**, 2415
- Takeuchi S., Ohsuga K., Mineshige S., 2013, *PASJ*, **65**, 88
- Tao L., Feng H., Grisé F., Kaaret P., 2011, *ApJ*, **737**, 81
- Titarchuk L., 1994, *ApJ*, **434**, 570
- Tortosa A., Bianchi S., Marinucci A., Matt G., Petrucci P. O., 2018, *A&A*, **614**, A37
- Tsunoda N., Kubota A., Namiki M., Sugiho M., Kawabata K., Makishima K., 2006, *PASJ*, **58**, 1081
- Vierdayanti K., Done C., Roberts T. P., Mineshige S., 2010, *MNRAS*, **403**, 1206
- Vinokurov A., Fabrika S., Atapin K., 2013, *Astrophysical Bulletin*, **68**, 139
- Vurm I., Poutanen J., 2009, *ApJ*, **698**, 293
- Walton D. J., Gladstone J. C., Roberts T. P., Fabian A. C., Caballero-Garcia M. D., Done C., Middleton M. J., 2011, *MNRAS*, **414**, 1011
- Walton D. J., Miller J. M., Harrison F. A., Fabian A. C., Roberts T. P., Middleton M. J., Reis R. C., 2013, *ApJ*, **773**, L9
- Walton D. J., et al., 2014, *ApJ*, **793**, 21
- Walton D. J., et al., 2015, *ApJ*, **806**, 65
- Walton D. J., et al., 2017, *ApJ*, **839**, 105
- Walton D. J., et al., 2018, *ApJ*, **856**, 128
- Wang Q. D., 2002, *MNRAS*, **332**, 764

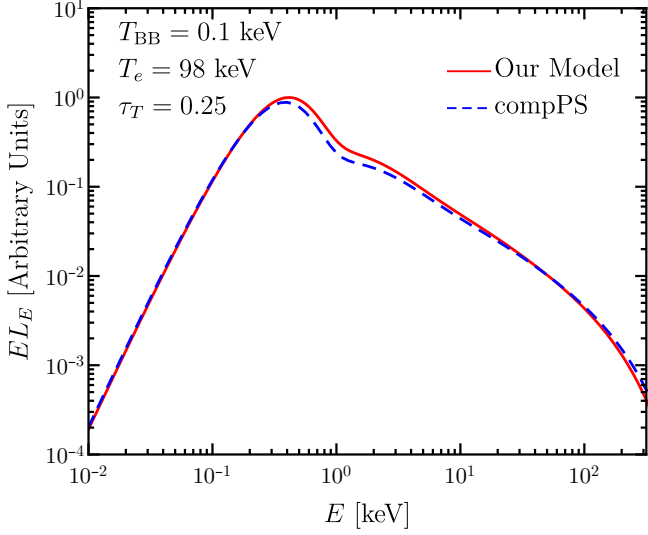


Figure A1. Model comparison with compPS using a simple thermal Comptonization setup.

Wilms J., Allen A., McCray R., 2000, *ApJ*, 542, 914

APPENDIX A: MODEL COMPARISON

Here we compare the thermally Comptonized spectrum from our model with CompPS (Poutanen & Svensson 1996), a popular Comptonization model from the literature that also uses the exact Compton scattering kernel producing more accurate spectra. CompPS uses blackbody (at temperature T_{BB}) or MCD emission for the seed photon spectrum and calculates the Comptonized emission for a thermal (at temperature T_e), power-law, or hybrid particle distribution. In that regard, the capabilities of our time-dependent numerical code are similar to CompPS, but the latter makes the steady state assumption that allows it to be computationally much less expensive. We compare the results from the two models in Fig. A1 for Thomson optical depth τ_T of the electrons and show that our model achieves good agreement with compPS.

APPENDIX B: MCMC MODEL FITS

To constrain the BH mass we carried out MCMC simulations using the python package emcee. The disk-corona model was used to fit only the X-ray data, and therefore no constraints were obtained for the f_{out} and \hat{R}_{out} parameters as they describe the irradiated disk component. These parameters are also degenerate given the sparse optical/UV data that is missing the spectral break near ~ 10 eV. This break is required to break the degeneracy.

The MCMC chains were constructed with $N_{\text{walker}} = 28$ and $N_{\text{steps}} = 200$ for each walker with a burn-in of 20 steps. Lowering N_{walker} by a factor of 2 and increasing N_{steps} by the same factor yields the same final result. Due to the computationally intensive nature of the numerical code used for producing the X-ray spectrum, the total number of steps had to be kept small. To ensure good sampling of the parameter distribution, a rule of thumb is to have a mean acceptance fraction between 0.2 and 0.5. In all the MCMC simulations we

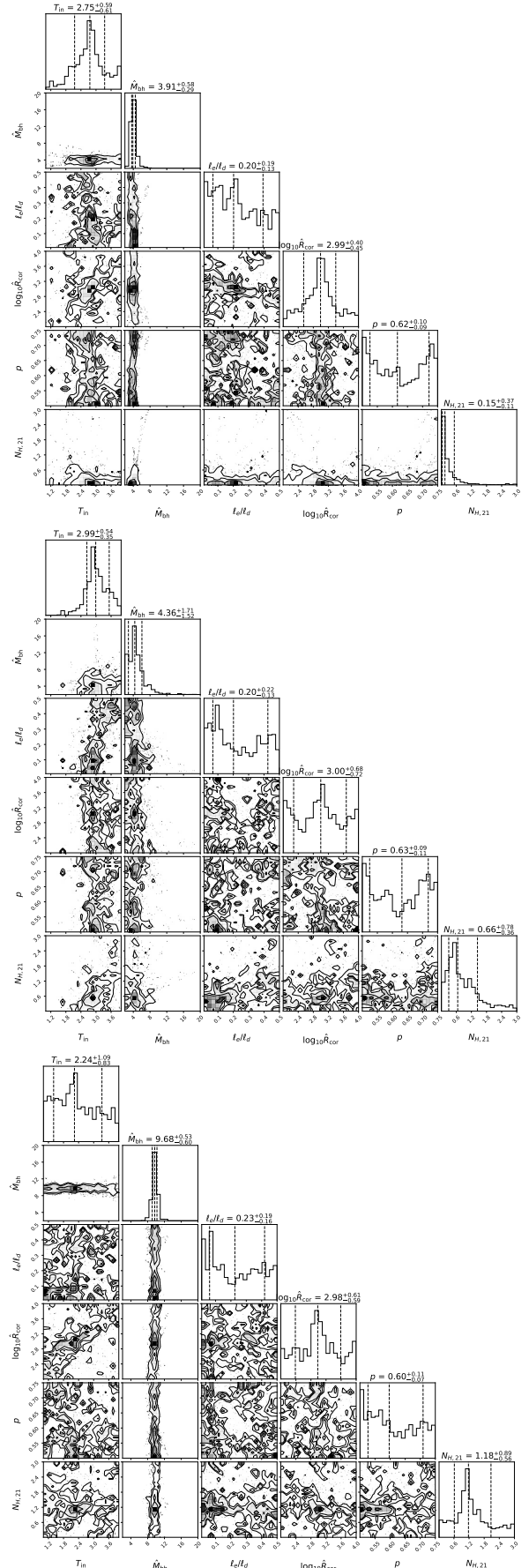


Figure B1. MCMC fit to the LOW (top), MEDIUM (middle), and HIGH (bottom) states. The posterior distributions are obtained with $N_{\text{walker}} = 28$ and $N_{\text{steps}} = 200$ for each walker with a mean acceptance fraction of 0.29.

find the mean acceptance fraction to be 0.29, which indicates good sampling.

From the posterior distributions, we find that the inner disk temperature, BH mass, and the size of the corona are well constrained in all the spectral states. Since our working assumption for the compact source is a BH, the probed mass range was limited from below at $\hat{M}_{\text{BH}} \geq 2$. The model parameters that are constrained most poorly are ℓ_e/ℓ_d and p due to some degeneracy in how they affect the X-ray spectrum.

This paper has been typeset from a $\text{\TeX}/\text{\LaTeX}$ file prepared by the author.